

Micro-scale continuous and discrete numerical models for nonlinear analysis of masonry shear walls

Massimo Petracca^{a,b,c,*}, Luca Pelà^{a,b}, Riccardo Rossi^{a,b}, Stefano Zaghi^{a,b}, Guido Camata^c, Enrico Spacone^c

^a*Department of Civil and Environmental Engineering, Universitat Politècnica de Catalunya (UPC-BarcelonaTech), Barcelona 08034, Spain*

^b*CIMNE - Centre Internacional de Metodes Numerics en Enginyeria, Universitat Politècnica de Catalunya (UPC-BarcelonaTech), Barcelona 08034, Spain*

^c*Department of Engineering, University "G.d'Annunzio" of Chieti and Pescara, Pescara 65127, Italy*

Abstract

A novel damage mechanics-based continuous micro-model for the analysis of masonry-walls is presented and compared with other two well-known discrete micro-models. The discrete micro-models discretize masonry micro-structure with nonlinear interfaces for mortar-joints, and continuum elements for units. The proposed continuous micro-model discretizes both units and mortar-joints with continuum elements, making use of a tension/compression damage model, here refined to properly reproduce the nonlinear response under shear and to control the dilatancy. The three investigated models are validated against experimental results. They all prove to be similarly effective, with the proposed model being less time-consuming, due to the efficient format of the damage model. Critical issues for these types of micro-models are analysed carefully, such as the accuracy in predicting the failure load and collapse mechanism, the computational efficiency and the level of approximation given by a 2D plane-stress assumption.

Keywords: Masonry, Continuous micro-modeling, Discrete micro-modeling, Continuum damage model, Interface model, Dilatancy

1. Introduction

Masonry is a composite material, with a micro-structure consisting of bricks and joints, with or without mortar. These micro-structural constituents, their very different elastic and inelastic properties, and their arrangement lead to very complex behaviors and different failure mechanisms. Several computational strategies were proposed to deal with the numerical analysis of such a complex material [1]. Several macro-models, also known as continuum finite element models, are available in the existing literature to study

*corresponding author

Email addresses: `m.petracca@cimne.upc.edu` (Massimo Petracca), `luca.pela@upc.edu` (Luca Pelà), `rrossi@cimne.upc.edu` (Riccardo Rossi), `zstefano@cimne.upc.edu` (Stefano Zaghi), `g.camata@unich.it` (Guido Camata), `espacone@unich.it` (Enrico Spacone)

masonry structures. The most recent macro-models regard the material as a fictitious homogeneous orthotropic continuum, without making any explicit distinction between units and joints in the discrete model [2, 3, 4]. This approach presents some intrinsic difficulties mainly related to the identification of the mechanical parameters of the continuum and the definition of realistic phenomenological failure criteria. However, macro-models are still a suitable option for the numerical analysis of large and complex structures due to their limited computational cost. More sophisticated numerical strategies were proposed by several authors for detailed analysis of single structural members, where a full description of the interaction between units and mortar is necessary (Figure 1a). Very popular approaches used nowadays to study masonry, including its heterogeneous micro-structure in the discretization, are based on micro-modeling [5, 6, 7, 8]. Midway between macro- and micro-modeling there are the homogenization methods [9, 10, 11, 12, 13, 14, 15, 16, 17, 18, 19].

A complete and detailed description of masonry micro-structure would require the full three-dimensional discretization of bricks, mortar joints, and the interface between them. In this way all masonry constituents and their complex interaction would be explicitly accounted for. However, three-dimensional modeling requires a complex model generation and high computational costs. For the case of a wall made of one layer of bricks with a regular pattern, the 2D plane stress assumption can be made to simplify the problem. This however can lead to imprecise results when the wall is subjected to high levels of compressions, since the state of triaxial compression in the mortar joints cannot be represented with the plane-stress assumption. A more accurate solution can be the adoption of generalized plane state [20, 21].

The objective of this paper is to propose a novel damage-mechanics based continuous micro-model able to represent the mechanical behaviors of masonry constituents. The proposed micro-model is based on a tension-compression continuum damage model [22, 23, 24], here refined in order to accurately reproduce the nonlinear response of masonry constituents, especially in shear. The adoption of appropriate failure criteria enables the analyst to control the dilatant behavior of the material, even though this aspect is not generally associated to continuum damage models as it is for plasticity models. The study proposes a simple solution to this issue, consisting in the appropriate definition of the failure surfaces under shear stress states together with the formulation of proper evolution laws for damage variables. For this aim, a failure criterion for quasi-brittle materials [25] is suitably enhanced under shear conditions and a novel hardening-softening law based on quadratic Bézier curves is established. The model keeps the simple and efficient format of classical damage models, where the explicit evaluation of the internal variables avoids nested iterative procedures, thus increasing computational performance and robustness. Another purpose of this research is to carry out a critical comparison of the proposed continuous micro-model with other two well-known discrete micro-modeling strategies for the numerical simulation of shear walls made of periodic masonry. The three micro-models explicitly take into account the interaction between units and mortar joints by including their separate discretizations. The main distinction made here between continuous and discrete micro-models is referred to the different type of elements and constitutive models used for the discretization of masonry micro-structure. Discrete micro-modeling has been widely adopted by several authors in literature [5, 7, 26, 27, 28, 29, 30] using a discrete description of masonry micro-structure, mixing continuum and interface elements for bricks and mortar joints, respectively. On the contrary, the proposed contin-

uous micro-modeling uses a continuum discretization of all components of the masonry micro-structure, without resorting to interface elements.

The investigated approaches are validated against experimental tests of masonry shear walls under different level of vertical compression [31], proving to be similarly effective and accurate in predicting the global strength of shear walls up to their collapse. All three micro-modeling techniques are able to properly reproduce the main failure mechanisms of the material, such as tensile cracking, sliding, shear and crushing. However, each one of the selected models introduces different approximations that lead to slight differences in accuracy, robustness and computational cost. The validation of the novel continuous micro-model, together with the critical review of available discrete micro-models, leads to a fruitful discussion on advanced computational strategies for the analysis of masonry structures at the level of material constituents.

2. Adopted modeling strategies

The three selected modeling strategies to represent the micro-structure of masonry material (see Figure 1a) are:

1. **2D Continuous micro-model (2D-C):** Both units and mortar joints are modeled using 2D plane-stress continuum elements with nonlinear behavior (see Figure 1b). This paper presents a novel formulation for this approach at the level of the constitutive law.
2. **2D Discrete micro-model (2D-D):** All non-linearity is lumped into interface elements. Both horizontal and vertical mortar joints are discretized by this type of elements. Units are composed of 2D continuum elastic elements and vertical interfaces at their mid-length for potential splitting cracks (see Figure 1c).
3. **2D Mixed Continuous/Discrete micro-model (2D-CD):** The mortar joints (vertical and horizontal) are represented by nonlinear interface elements, whereas the units are modeled with 2D plane-stress continuum elements with nonlinear behavior, to avoid forcing the crack pattern inside the units, differently from 2D-D approach (see Figure 1d).

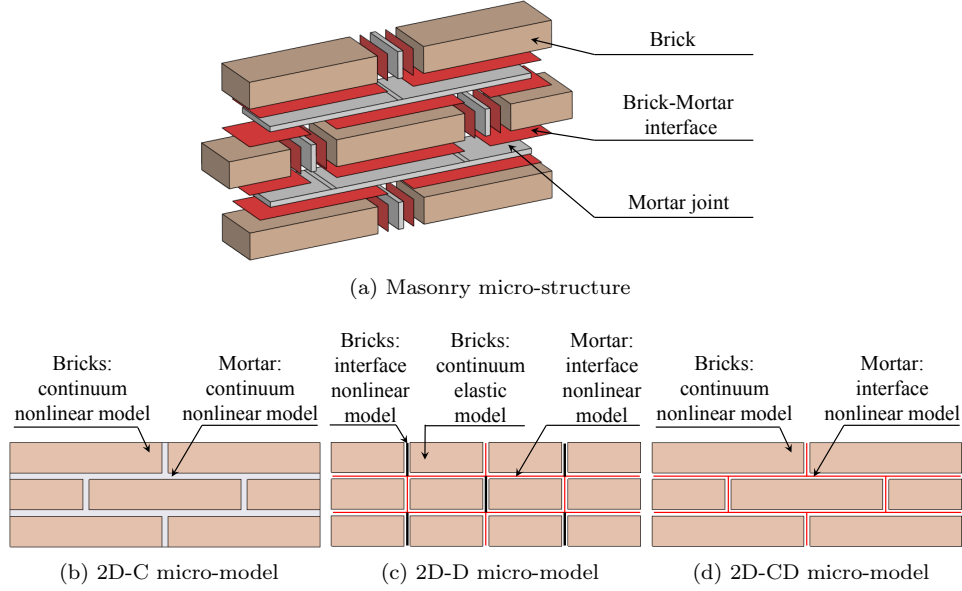


Figure 1: Masonry modeling strategies

The aforementioned 2D-D and 2D-CD micro-modeling strategies for masonry structures are very well-known and they have been used by several authors in the available literature [5, 7, 26, 27, 28, 29, 30]. In the present comparative study, the adopted constitutive model for the interfaces is the one presented in [5]. The 2D-D and 2D-CD strategies are also known as "simplified micro-models", while "detailed micro-models" would consider a distinct discretization for units and mortar (by means of continuum finite elements) and unit-mortar interface (by means of interface elements).

On the other hand, the proposed 2D-C micro-modeling strategy considers a more classical approach, discretizing both bricks and mortar joints with continuum elements. In this context, and to propose an efficient and robust numerical method, a constitutive law based on continuum damage mechanics is adopted, taking advantage of its explicit evaluation, thus avoiding local iterative procedures typically necessary to integrate plasticity-based models. In particular, the d^+/d^- tension-compression damage framework [22, 23, 24] has been used. This model introduces two failure criteria for tensile and compressive stress states, as well as two scalar damage indexes, allowing the description of different behaviors under tension and compression. A novel failure criterion for compression is presented in Section 3.2 to be combined with a novel hardening-softening law based on quadratic Bézier curves (Section 3.3). Section 4 describes how this criterion can be used to control the dilatant behavior of the damage model.

In the following, Section 3 describes the continuum damage model here proposed, and used for both bricks and mortar joints in the modeling strategy 2D-C, and for bricks in the modeling strategy 2D-CD, while Section 5 describes the constitutive model used for mortar interfaces in the modeling strategies 2D-D and 2D-CD.

Note that the modeling strategy 2D-CD features both a plasticity-based model (in mortar joints), and a damage-based one (in bricks). The choice of a damage model for bricks stems from the brittle nature of bricks failure mechanism. In fact, in in-plane loaded shear walls, the main failure mechanism that can be expected at the brick level is a brittle tensile split, which can be accurately represented by a damage model.

3. Proposed Tension/Compression Continuum Damage Model

3.1. Constitutive Model

The 2-parameter d^+/d^- damage model, based on the works in [22, 23, 24], defines the stress tensor as

$$\boldsymbol{\sigma} = (1 - d^+) \bar{\boldsymbol{\sigma}}^+ + (1 - d^-) \bar{\boldsymbol{\sigma}}^- \quad (1)$$

where $\bar{\boldsymbol{\sigma}}$ is the effective (elastic) stress tensor

$$\bar{\boldsymbol{\sigma}} = \mathbf{C} : \boldsymbol{\varepsilon} \quad (2)$$

while $\bar{\boldsymbol{\sigma}}^+$ and $\bar{\boldsymbol{\sigma}}^-$ are, respectively, its positive and negative components, computed as:

$$\bar{\boldsymbol{\sigma}}^+ = \sum_{i=1}^3 \langle \bar{\sigma}_i \rangle \mathbf{p}_i \otimes \mathbf{p}_i \quad (3)$$

$$\bar{\boldsymbol{\sigma}}^- = \bar{\boldsymbol{\sigma}} - \bar{\boldsymbol{\sigma}}^+ \quad (4)$$

d^+ and d^- are tensile and compressive damage indexes, affecting, respectively, the positive $\bar{\boldsymbol{\sigma}}^+$ and negative $\bar{\boldsymbol{\sigma}}^-$ components of the effective stress $\bar{\boldsymbol{\sigma}}$. These damage indexes are scalar variables ranging from 0 (intact material) to 1 (completely damaged material).

3.2. Failure Criteria

Two scalar measures, referred to as equivalent stresses τ^+ and τ^- , are introduced to properly identify “loading”, “unloading” or “reloading” conditions.

The compressive surface employed in this research represents an improvement of the one described in [25]. The equivalent stress τ^- is computed as

$$\tau^- = \frac{1}{1 - \alpha} \left(\alpha \bar{I}_1 + \sqrt{3 \bar{J}_2} + k_1 \beta \langle \bar{\sigma}_{max} \rangle \right) \quad (5)$$

$$\alpha = \frac{k_b - 1}{2k_b - 1} \quad (6)$$

$$\beta = \frac{f_{cp}}{f_t} (1 - \alpha) - (1 + \alpha) \quad (7)$$

where \bar{I}_1 is the first invariant of the effective stress tensor, \bar{J}_2 is the second invariant of the effective deviatoric stress tensor, $\bar{\sigma}_{max}$ is the maximum effective principal stress, f_{cp} is the compressive peak stress and k_b is the ratio of the bi-axial strength to the uniaxial strength in compression. The constant k_1 in Eq. (5) is proposed in this research to control the influence that the compressive criterion has on the dilatant behavior of the model, as described in Section 4. k_1 ranges from 0 to 1. A value of 0 leads to the Drucker-Prager criterion, while a value of 1 leads to the criterion presented in [25]), as shown in Figure 2.

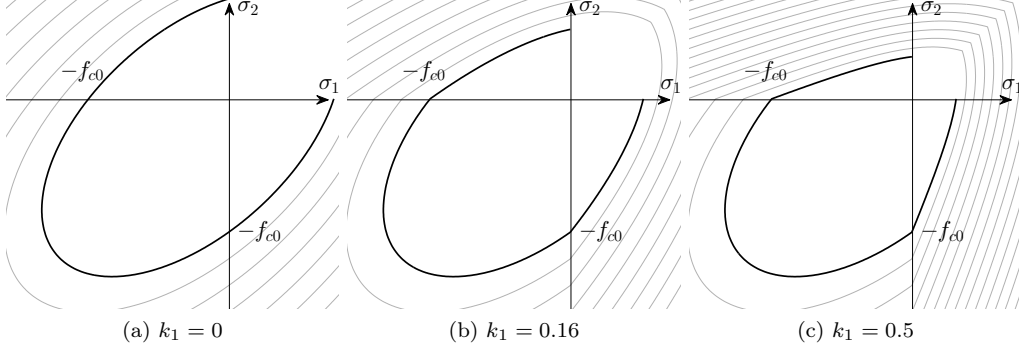


Figure 2: Proposed compressive failure surface for the continuum model. Influence of the parameter k_1

The tensile surface is similar to the compressive one

$$\tau^+ = \frac{1}{1-\alpha} \left(\alpha \bar{I}_1 + \sqrt{3\bar{J}_2} + \beta \langle \bar{\sigma}_{max} \rangle \right) \frac{f_t}{f_{cp}} \quad (8)$$

but without the k_1 parameter. Here the term $\frac{f_t}{f_{cp}}$ is introduced to compare τ^+ with the uniaxial tensile strength f_t . Figure 3 shows the two initial damage surfaces, for the plane-stress case, superimposed in the principal stress space. The negative surface τ^- is represented for various values of the constant k_1 . Being the two surfaces defined for any state of stress, it may happen that negative damage evolves under uniaxial or biaxial tension and vice-versa for the tensile damage. This can be avoided inactivating the tensile and compressive criteria under conditions, so that (i) the compressive surface can evolve if and only if at least one of the principal stresses is negative, and (ii) the tensile surface can evolve if and only if at least one the principal stresses is positive.

These conditions can be taken into account by rewriting the damage surfaces as:

$$\tau^- = H(-\bar{\sigma}_{min}) \left[\frac{1}{1-\alpha} \left(\alpha \bar{I}_1 + \sqrt{3\bar{J}_2} + k_1 \beta \langle \bar{\sigma}_{max} \rangle \right) \right] \quad (9)$$

$$\tau^+ = H(\bar{\sigma}_{max}) \left[\frac{1}{1-\alpha} \left(\alpha \bar{I}_1 + \sqrt{3\bar{J}_2} + \beta \langle \bar{\sigma}_{max} \rangle \right) \frac{f_t}{f_{cp}} \right] \quad (10)$$

where $H(x)$ is the Heaviside function, defined as

$$H(x) = \begin{cases} 0 & x < 0 \\ 1 & x > 0 \end{cases} \quad (11)$$

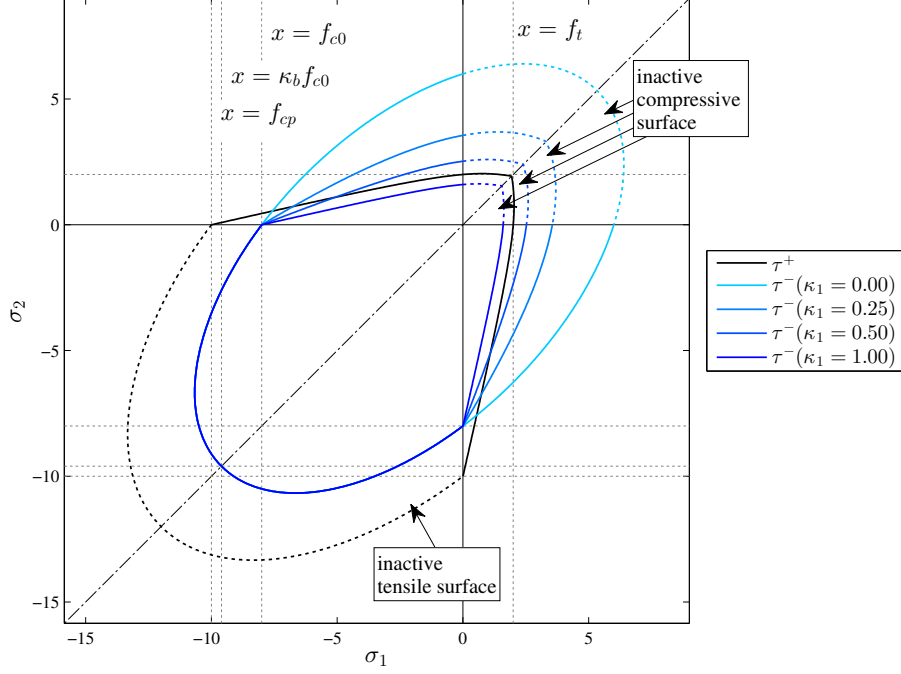


Figure 3: Initial damage surfaces for the plane-stress case.

To account for the irreversible nature of damage, two scalar quantities are used, referred to as damage thresholds r^\pm . The thresholds r^\pm denote the largest values attained by the equivalent stresses τ^\pm throughout the whole loading history up to the current time instant. r^\pm at time $t + \Delta t$ are explicitly evaluated as

$$r^\pm = \max \left(r_0^\pm, \max_{0 \leq n \leq t} \tau_n^\pm \right)$$

$$r_0^+ = f_t \quad (12)$$

$$r_0^- = f_{c0} \quad (13)$$

with r_0^+ and r_0^- being the initial damage thresholds, i.e. the elastic limits in uniaxial tension f_t and uniaxial compression f_{c0} . n denotes the time instant. With τ^\pm and r^\pm at hand, the damage criteria can be defined as:

$$\Phi(\tau^\pm, r^\pm) = \tau^\pm - r^\pm \leq 0 \quad (14)$$

3.3. Evolution laws for damage variables

The tensile (positive) damage d^+ is obtained from the following exponential softening law (see Figure 4):

$$d^+(r^+) = 1 - \frac{r_0^+}{r^+} \exp \left\{ 2H_{dis} \left(\frac{r_0^+ - r^+}{r_0^+} \right) \right\} \quad (15)$$

where H_{dis} is the discrete softening parameter. In the discrete problem, in order to achieve invariance of the response with respect to the discretization size, the softening law must be modified according to the size of the damaging zone (l_{dis}) [32, 33, 34], so that the following equation holds:

$$g_f l_{dis} = G_f \quad (16)$$

where G_f is the fracture energy per unit area in tension. The specific fracture energy g_f per unit volume, for the exponential softening law, is obtained as:

$$g_f = \left(1 + \frac{1}{H_{dis}} \right) \frac{f_t^2}{2E} \quad (17)$$

The discrete softening parameter H_{dis} is given by

$$H_{dis} = \frac{l_{dis}}{l_{mat} - l_{dis}} \quad (18)$$

where $l_{mat} = 2EG_f/f_t^2$. l_{dis} is taken equal to the characteristic size of the finite element ($l_{dis} = l_{ch}$).

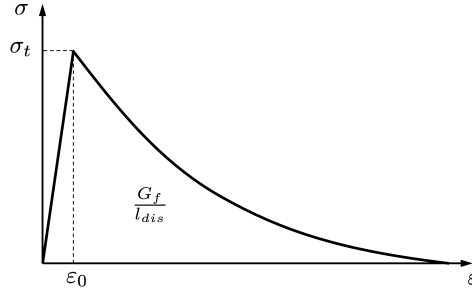


Figure 4: Tensile uniaxial law

The evolution of the compressive damage index d^- , instead, is governed by an ad hoc uniaxial law proposed in this paper, as shown in Figure 5.

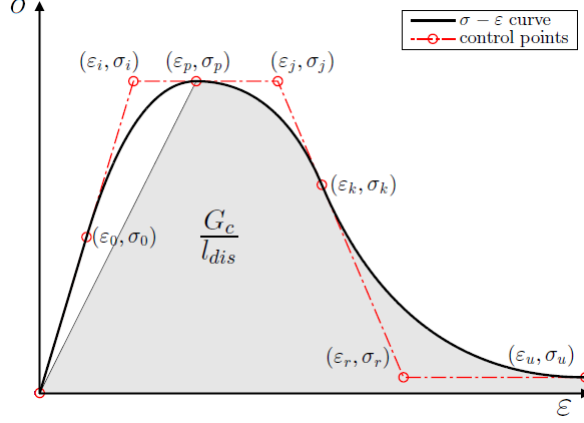


Figure 5: Compressive uniaxial law

This curve is made of a linear part $[(0, 0) - (\varepsilon_0, \sigma_0)]$, a hardening part $[(\varepsilon_0, \sigma_0) - (\varepsilon_p, \sigma_p)]$ and two softening parts $[(\varepsilon_p, \sigma_p) - (\varepsilon_k, \sigma_k)]$ $[(\varepsilon_k, \sigma_k) - (\varepsilon_u, \sigma_u)]$, followed by a final residual plateau $[(\varepsilon_u, \sigma_u) - (+\infty, \sigma_u)]$.

The hardening and softening portions are three quadratic Bézier curves. Each one of them has three control points that define their shape, the end-positions, and the tangents to the curve at the end-positions.

We can define a function \mathcal{B} that evaluates the Y-coordinate of a Bézier curve at a given X-abscissa, given the three control points, as follows:

$$\mathcal{B}(X, x_1, x_2, x_3, y_1, y_2, y_3) = (y_1 - 2y_2 + y_3)t^2 + 2(y_2 - y_1)t + y_1 \quad (19)$$

where

$$\begin{aligned} A &= x_1 - 2x_2 + x_3 \\ B &= 2(x_2 - x_1) \\ C &= x_1 - X \\ D &= B^2 - 4AC \\ t &= \frac{-B + \sqrt{D}}{2A} \end{aligned}$$

Given the current compressive damage threshold r^- , its strain-like counterpart ξ can be obtained

$$\xi = \frac{r^-}{E} \quad (20)$$

and then it is used to calculate the corresponding hardening variable $\Sigma(\xi)$:

$$\Sigma(\xi) = \begin{cases} \mathcal{B}(\xi, \varepsilon_0, \varepsilon_i, \varepsilon_p, \sigma_0, \sigma_i, \sigma_p) & \varepsilon_0 < \xi \leq \varepsilon_p \\ \mathcal{B}(\xi, \varepsilon_p, \varepsilon_j, \varepsilon_k, \sigma_p, \sigma_j, \sigma_k) & \varepsilon_p < \xi \leq \varepsilon_k \\ \mathcal{B}(\xi, \varepsilon_k, \varepsilon_r, \varepsilon_u, \sigma_k, \sigma_r, \sigma_u) & \varepsilon_k < \xi \leq \varepsilon_u \\ \sigma_u & \xi > \varepsilon_u \end{cases} \quad (21)$$

Finally the damage index d^- can be calculated as follows:

$$d^-(r^-) = 1 - \frac{\Sigma(\xi)}{r^-} \quad (22)$$

This novel formulation for the evolution law of the compressive damage parameter d^- is more flexible than conventional ones. In fact, the control points of the Bézier curves may be set so that the curve can match the experimental response obtained from an uniaxial compressive test. Then the compressive fracture energy G_c (shaded area in Figure 5) is evaluated with the following relations:

$$G_{c,1} = \frac{\sigma_p \varepsilon_p}{2} \quad (23)$$

$$G_{c,2} = \mathcal{G}(\varepsilon_p, \varepsilon_j, \varepsilon_k, \sigma_p, \sigma_j, \sigma_k) \quad (24)$$

$$G_{c,3} = \mathcal{G}(\varepsilon_k, \varepsilon_r, \varepsilon_u, \sigma_k, \sigma_r, \sigma_u) \quad (25)$$

$$G_c = G_{c,1} + G_{c,2} + G_{c,3} \quad (26)$$

where the area \mathcal{G} under each Bézier curve reads:

$$\mathcal{G}(x_1, x_2, x_3, y_1, y_2, y_3) = \frac{x_2 y_1}{3} + \frac{x_3 y_1}{6} - \frac{x_2 y_3}{3} + \frac{x_3 y_2}{3} + \frac{x_3 y_3}{2} - x_1 \left(\frac{y_1}{2} + \frac{y_2}{3} + \frac{y_3}{6} \right) \quad (27)$$

It should be noted that here G_c is not the total area under the uniaxial curve, but only the portion that needs to be regularized (post-peak regime).

In the discrete problem the compressive curve shown in Figure 5 needs to be regularized so that the shaded area underneath be G_c/l_{dis} . This can be achieved by “*stretching*” the strain abscissas ε_j , ε_k , ε_r and ε_u (before using them in Eq. (21)):

$$\tilde{\varepsilon}_\alpha = \varepsilon_\alpha + \mathcal{S}(\varepsilon_\alpha - \varepsilon_p), \quad \alpha = j, k, r, u \quad (28)$$

where \mathcal{S} is a stretching factor calculated as

$$\mathcal{S} = \frac{\frac{G_c}{l_{dis}} - G_{c,1}}{G_c - G_{c,1}} - 1 \quad (29)$$

This factor should be greater than -1.0 to avoid a constitutive snap-back. In fact for a stretch factor $\mathcal{S} = -1.0$ every post-peak strain-abscissa would collapse to the peak strain ε_p , leading to a sudden fall of the uniaxial curve. To avoid this, the characteristic length l_{dis} should satisfy the following restriction:

$$l_{dis} < \frac{2G_c}{\sigma_p \varepsilon_p} \quad (30)$$

The effect of this regularization on the uniaxial law can be seen in Figure 6.

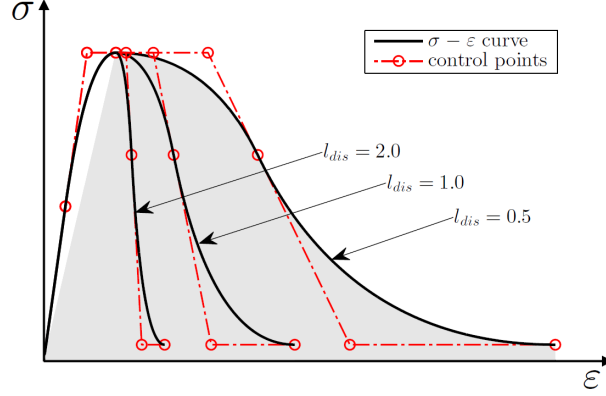


Figure 6: Regularization of compressive uniaxial law

4. Shear behavior and dilatancy of the Tension/Compression Continuum Damage Model

This section describes the shear behavior of the proposed d^+/d^- damage model. The present formulation includes the possibility to calibrate the dilatant behavior of the material under shear stresses. This crucial aspect has been usually disregarded by available models based on classical damage mechanics theory. Such disadvantage has often favored the use of plasticity models since they can control explicitly the dilatancy through the definition of a proper plastic potential. This work proposes an improvement of the well-known d^+/d^- damage model [22, 23, 24] to control the dilatant behavior of the material. The material dilatancy is described without resorting to the formulation of a plastic potential, i.e. differently from well-established plasticity models (e.g. Eq. (36)). The objective of the proposed approach is to describe phenomenologically the dilatant behavior without spoiling the simple and efficient format of the classical damage mechanics models.

4.1. Shear response of the Tension/Compression Damage Model

The models adopted in this paper are based on the 2D plane stress hypothesis. In this specific case, and in the framework of the d^+/d^- damage model, when the two principal stresses have different sign, both tensile and compressive surfaces might be active. In this case the positive principal stress is affected by the tensile damage while the minimum principal stress is affected by the compressive damage. If the damage was isotropic, i.e. the tension and compression damage variables are equal, the damaged stress tensor would

be an isotropic scaling of the effective (elastic) stress tensor. On the other hand, in the d^+/d^- damage model the damaged stress tensor is actually obtained by an anisotropic scaling of the effective (elastic) stress tensor, as it was already demonstrated in [2].

Figure 7 graphically shows this behavior for the simple case of a pure shear distortion, in an isotropic damage model (Figure 7a) and d^+/d^- damage model (Figure 7b). Let us suppose that the material point is subject to a given strain state whose components are $(\varepsilon_{xx} = 0, \varepsilon_{yy} = 0, \gamma_{xy} \neq 0)$. Point *A* represents the effective stress state $\bar{\sigma} = \mathbf{C} : \varepsilon$ due to pure shear, with coordinates $(\bar{\sigma}_1, \bar{\sigma}_2 = -\bar{\sigma}_1)$ in the principal stresses reference system. Point *B* represents the damaged stress state σ denoted by coordinates $(\sigma_1, \sigma_2 = -\sigma_1)$ obtained in the case of an isotropic damage model, i.e. if $d^+ = d^-$. In this case the damaged stress tensor is an isotropic scaling of the effective stress tensor, since the isotropic scalar damage index scales the whole effective stress tensor $\bar{\sigma}$. Consequently the damaged stress would stay in a pure shear state as the effective stress (Figure 7a). Point *C*, instead, corresponds to the damaged stress σ obtained by the d^+/d^- damage model. In this case, due to the existence of two different failure surfaces, the tensile and compressive damage indexes do not have in general the same value, being their evolution laws different. Consequently the damaged stress is not an isotropic scaling of the effective stress. In the specific example depicted in Figure 7b, the compressive damage increment is smaller than the tensile one. Thus, due to the preassigned null values for ε_{xx} and ε_{yy} , the damaged stress σ must denote a shear-compression state.

In the compressive damage surface in Eq. (5), the parameter k_1 is introduced to control the “weight” of the compressive surface on the constitutive shear response in the nonlinear range. As shown in Figure 2, the parameter k_1 controls the size of the compressive surface in tension/compression quadrants. As a consequence, this parameter controls implicitly also the dilatancy of the model, taking into account that the larger the compressive surface (with respect to the tensile surface), the higher the dilatancy. This effect is shown in Figure 8 for decreasing values of k_1 , moving from Figure 8a to Figure 8c. It can be seen how decreasing k_1 from 1 to 0, the size of the compressive surface in the tension/compression quadrants increases. As a consequence, the increment of the compressive damage index d^- diminishes, thus predicting increasing compressive stresses.

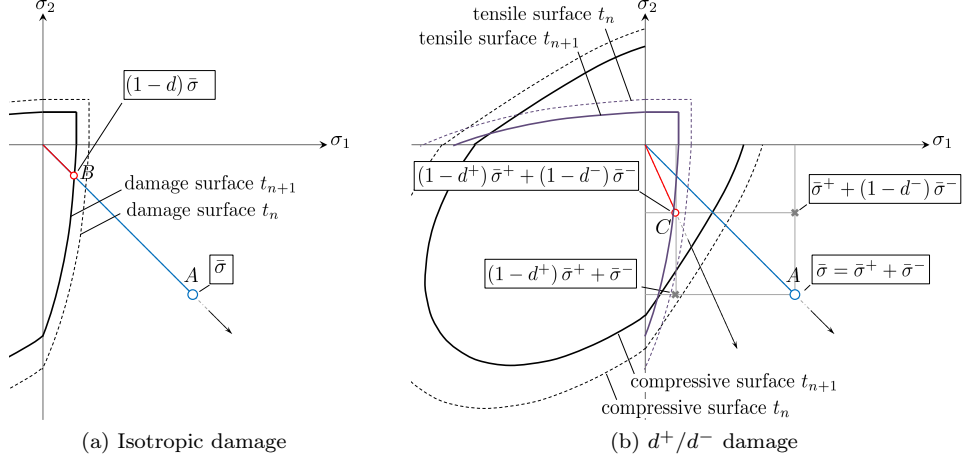


Figure 7: Behavior of isotropic and d^+/d^- damage models in tension/compression quadrants

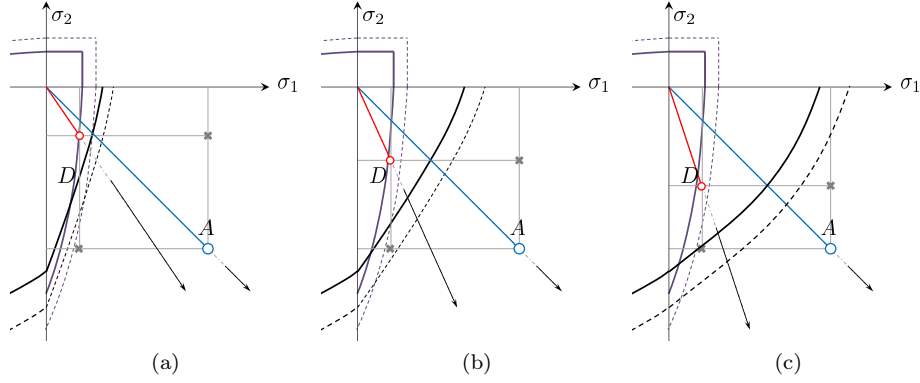


Figure 8: Behavior of d^+/d^- damage model in tension/compression quadrants for values of k_1 decreasing from (a) to (c)

4.2. Numerical modeling of shear behavior of mortar joints

To assess the performance of the proposed constitutive model in shear, the experimental shear tests conducted in [35] are numerically reproduced here. Figure 9a shows the test set-up. These tests aim at producing a constant stress state in the mortar joint. Mortar joints are subjected to shear under a constant confining stress.

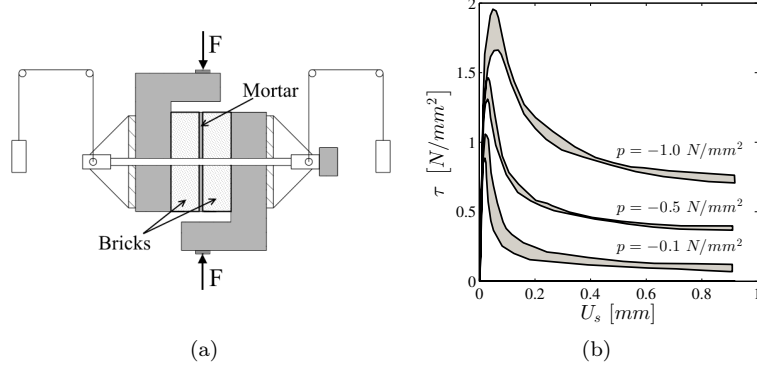


Figure 9: Van Der Pluijm (1993). (a) test set-up; (b) test results for different values of confinement

The experimental tests were conducted with three different confining stress levels of -0.1 , -0.5 and -1.0 N/mm². Experimental results are given in Figure 9b in terms of envelope curves of shear stress τ vs. shear displacement U_s along the mortar joint. It can be seen how the maximum shear stress increases with increasing confining stress. After reaching a peak value, the shear stress decreases with increasing shear displacement, reaching a residual value due to dry friction. Another important aspect of this kind of experiment is the dilatancy of the mortar joint (Figure 10a), which describes the appearance (in the nonlinear range) of normal displacement perpendicular to the shear displacement. The ratio between the normal and shear displacements is denoted as the tangent to the dilatancy angle ψ . This behavior is related to the roughness of the crack surface. Experimental results show how dilatancy decreases with increasing normal stresses, as shown in Figure 10b. In the same way, for a constant normal stress, the dilatancy decreases to zero upon increasing shear displacement, as shown in Figure 10c.

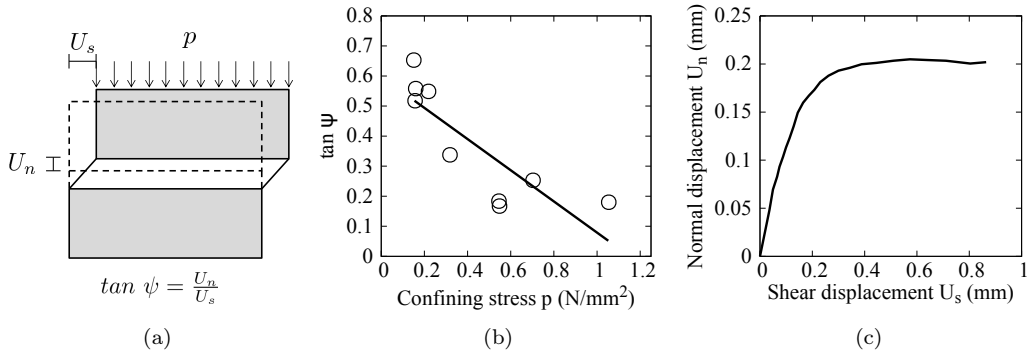


Figure 10: Van Der Pluijm (1993). (a) dilatancy of mortar joints; (b) dilatancy $\tan \psi$ as a function of confining stress; (c) typical evolution of normal displacement for increasing values of shear displacement. Adapted from [6].

To study the control of the dilatancy in the proposed model, an elemental test has been performed. The geometry and boundary conditions are shown in Figure 11. Material parameters, obtained from [35], are given in Table 1. For each level of confining stress ($p = -0.1$, $p = -0.5$, and $p = -1.0 \text{ N/mm}^2$) two analyses have been conducted, using $k_1 = 0$, and $k_1 = 0.16$. The value $k_1 = 0.16$ has been found as optimal for these tests as well as for the shear walls analyzed in Section 6.

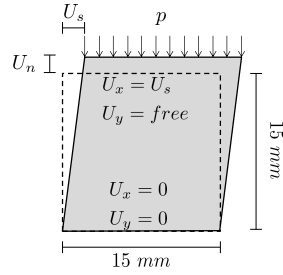


Figure 11: Elemental shear test. Geometry and boundary conditions

E	ν	σ_t	G_t	σ_0	σ_p	σ_r	G_c	ε_p	k_b
2970.0	0.15	0.62	0.02	8.0	11.0	1.0	20.0	0.005	1.16
$\frac{\text{N}}{\text{mm}^2}$	-	$\frac{\text{N}}{\text{mm}^2}$	$\frac{\text{N}}{\text{mm}}$	$\frac{\text{N}}{\text{mm}^2}$	$\frac{\text{N}}{\text{mm}^2}$	$\frac{\text{N}}{\text{mm}^2}$	$\frac{\text{N}}{\text{mm}}$	-	-

Table 1: Mortar material properties for the shear tests

Results of the analyses are given in Table 2 in terms of shear strength and dilatancy, for each level of pre-compression. The first column show the shear stress - shear displacement curves, with the shear strength increasing for higher values of pre-compression. The second column show the uplift (positive vertical displacement) generated upon shear displacement. Finally the third column shows the dilatancy coefficient (which is the tangent to the curves reported in the second column). It can be clearly seen that if the standard Drucker-Prager failure surface ($k_1 = 0$) is chosen for compression, an overestimation of the dilatant behavior (with respect to the values shown in Figure 10b and Figure 10c) is obtained.

Overall, these analyses show how the size of the compressive surface in the tension/compression quadrants has a major impact on the dilatancy of the model. As explained in the introduction of this section, the d^+/d^- damage model as proposed in [22, 23, 24] does not explicitly impose the direction of the inelastic strain, as opposed to plastic models. This elemental test has shown how a careful definition of the compressive damage surface, and

especially of its shape in the II and IV quadrants of the principal (plane)stress space, can help in controlling the dilatant behavior in the proposed continuum damage model. It can be noticed, however, that for higher levels of vertical compression, the maximum shear strength is slightly underestimated (see Table 2, case $p=-1$ N/mm²). The same effect will be found in the results of the analysis of the shear walls given in Section 6.2. This slight underestimation may be due to the limitations given by plane-stress assumption. In fact, for high levels of compression, the plane-stress hypothesis is not able to represent the triaxial compression state in the mortar bed joint given by its interaction with the surrounding units.

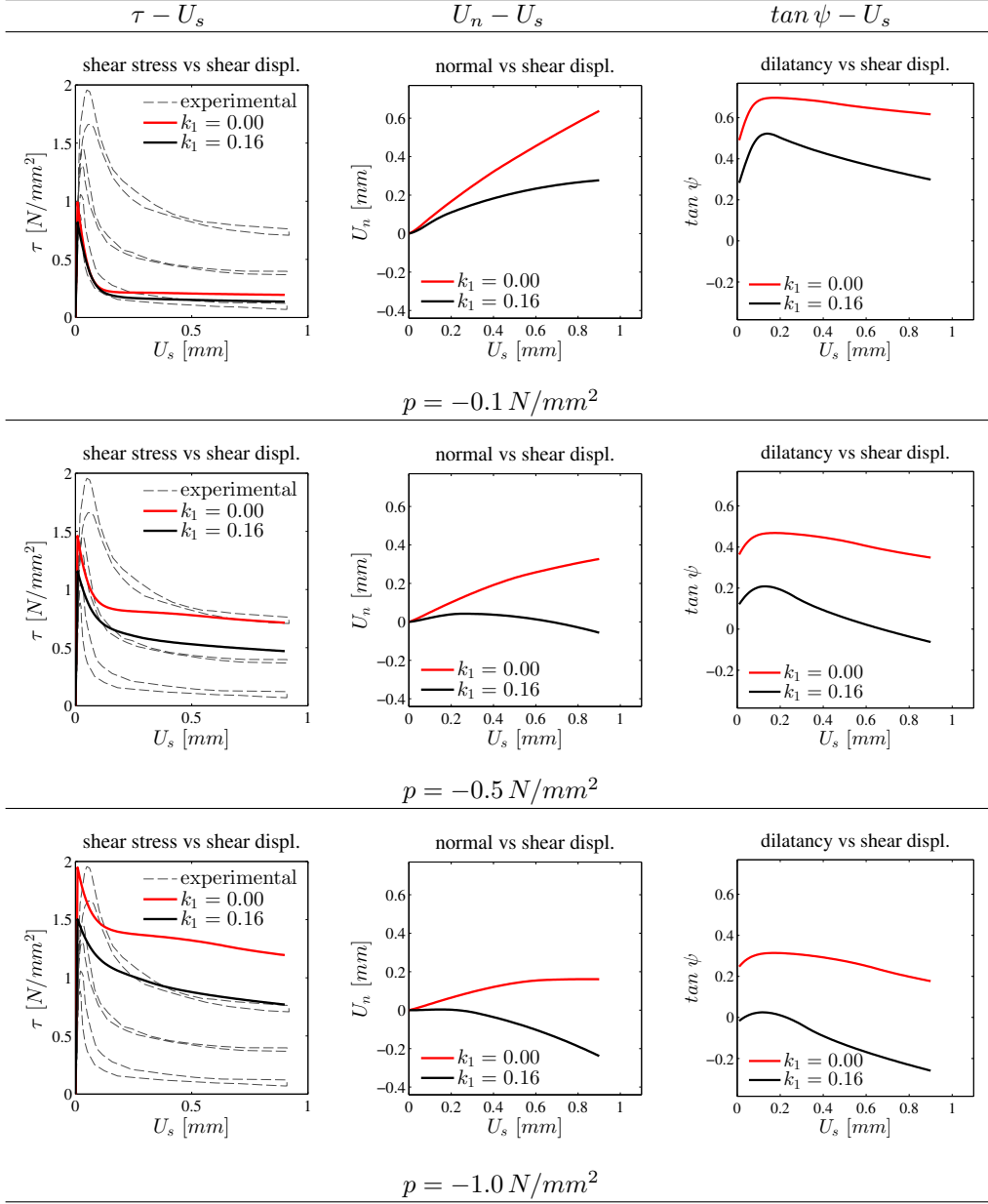


Table 2: Numerical results of the elemental shear test

5. Multisurface Plasticity Interface Model

Mortar joints are modeled using interface elements, allowing to incorporate discontinuities in the displacement field. Thus a constitutive law in terms of relative displacement and traction vector is required. The constitutive model adopted in this work is the one formulated in [5]. For the sake of completeness, only a brief description of the model is given here, and for further details the reader should refer to [5]. This model is based on the concept of multisurface plasticity to better describe all failure mechanisms of masonry, through the definition of three surfaces for tension, shear and compressive failures, as shown in Figure 12.

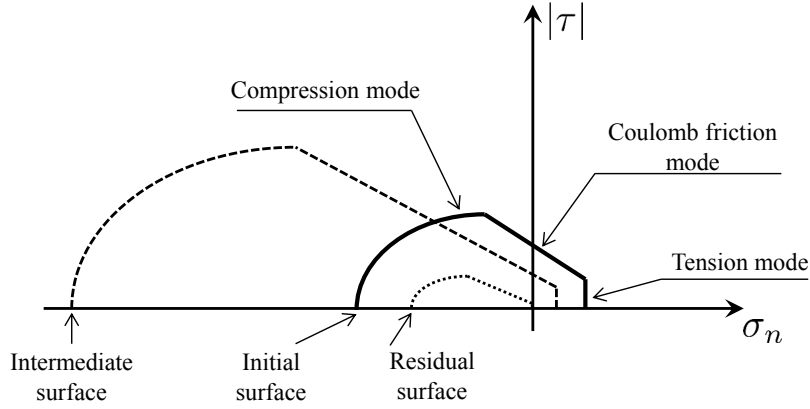


Figure 12: Composite yield surface for mortar joints, from [5].

For an interface element, the elastic response relating the generalized stresses $\boldsymbol{\sigma} = \{\sigma_n, \tau\}^T$ and the generalized strains $\boldsymbol{\varepsilon} = \{u_n, u_s\}^T$ is given by

$$\boldsymbol{\sigma} = \mathbf{D}\boldsymbol{\varepsilon} = \text{diag}\{k_n, k_s\}\boldsymbol{\varepsilon} \quad (31)$$

where k_n and k_s are the stiffness parameters (not meant as dummy stiffnesses to simulate contact) in the normal and tangential directions, and can be obtained by the elastic properties of brick and mortar as follows:

$$k_n = \frac{E_b E_m}{t_m (E_b - E_m)}; \quad k_s = \frac{G_b G_m}{t_m (G_b - G_m)} \quad (32)$$

where E_b , E_m , t_m , G_b , G_m are respectively the brick Young's modulus, the mortar Young's modulus, the mortar thickness, the brick Shear modulus and the mortar Shear modulus. To describe the nonlinear regime, three yield functions are employed in the framework of multisurface plasticity:

$$f_1(\boldsymbol{\sigma}, \kappa_1) = \sigma_n - f_t(\kappa_1) \quad (33)$$

$$f_2(\boldsymbol{\sigma}, \kappa_2) = |\tau| + \sigma_n \tan \phi(\kappa_2) - c(\kappa_2) \quad (34)$$

$$f_3(\boldsymbol{\sigma}, \kappa_3) = C_{nn}\sigma_n^2 + C_{ss}\tau^2 + C_n\sigma_n - f_c(\kappa_3)^2 \quad (35)$$

f_1 is the tension cut-off criterion, where $f_t(\kappa_1)$ is the yield value and k_1 is the hardening-softening parameter. Associated flow rule is considered.

f_2 is the Coulomb friction criterion, where $c(\kappa_2)$ is the cohesion, $\phi(\kappa_2)$ is the friction angle, and k_2 is the hardening-softening parameter. To properly describe dilatancy in mortar joints, a non-associated flow rule is considered, replacing the friction angle with the dilatancy angle ψ :

$$g_2(\boldsymbol{\sigma}, \kappa_2) = |\tau| + \sigma_n \tan \psi(\kappa_2) - c(\kappa_2) \quad (36)$$

f_3 is the elliptical cap criterion, where $f_c(\kappa_3)$ is the yield value and k_3 is the hardening/softening parameter. C_{nn} , C_{ss} and C_n are parameters describing the shape of the elliptical cap. An associated flow rule is assumed.

The evolution of the yield value f_t is described by an exponential softening:

$$f_t(\kappa_1) = f_{t0} \exp\left(-\frac{f_{t0}}{G_f^I} \kappa_1\right) \quad (37)$$

where f_{t0} is the initial tensile strength and G_f^I is the tensile fracture energy. Similarly, the evolution of the cohesion is given by same exponential softening:

$$c(\kappa_2) = c_0 \exp\left(-\frac{c_0}{G_f^{II}} \kappa_2\right) \quad (38)$$

where c_0 is the initial cohesion and G_f^{II} is the shear fracture energy. The evolution of friction and dilatancy angles is linked to the evolution of the cohesion:

$$\tan \phi(\kappa_2) = \tan \phi_0 + (\tan \phi_r - \tan \phi_0) \left(\frac{c_0 - c}{c_0}\right) \quad (39)$$

$$\tan \psi(\kappa_2) = \tan \psi_0 + (\tan \psi_r - \tan \psi_0) \left(\frac{c_0 - c}{c_0}\right) \quad (40)$$

where ϕ_0 and ψ_0 are the initial friction and dilatancy angles, while ϕ_r and ψ_r are the residual friction and dilatancy angles.

The evolution of $f_c(\kappa_3)$ is described by a hardening-softening law in terms of plastic displacements, explained in Section 3.2.

6. Numerical modeling of shear walls

The adopted modeling strategies are used to model the experimental response of masonry shear walls [31]. Section 6.1 describes the experimental tests, then the results of each modeling strategy is described in detail. Finally, Section 6.5 compares the adopted modeling strategies, highlighting similarities/differences and advantages/disadvantages. The analyses were performed using an enhanced version of the software Kratos Multi-physics [36, 37], while pre- and post-processing were done with GiD [38].

6.1. Numerical simulation of experimental test: TU Eindhoven shear wall

The geometry and boundary conditions of the wall are given in Figure 13. The wall consists of single layer of solid bricks ($210\text{ mm} \times 52\text{ mm} \times 100\text{ mm}$), and 10 mm of mortar [31]. Loading conditions are applied in two stages. In the first stage, the top of the wall is subjected to a uniform vertical compression. In the second stage, a horizontal force is applied via displacement control, while keeping the top of the wall horizontal. The test is performed for three increasing values of vertical compression (0.30 , 1.21 and 2.12 N/mm^2). The experimentally obtained crack patterns are shown in Figure 14. Two tests were carried out only for a pre-compression level of 0.3 N/mm^2 , and the envelope of their load-displacement curves is represented as a shaded area in Figure 15, Figure 17 and Figure 18.

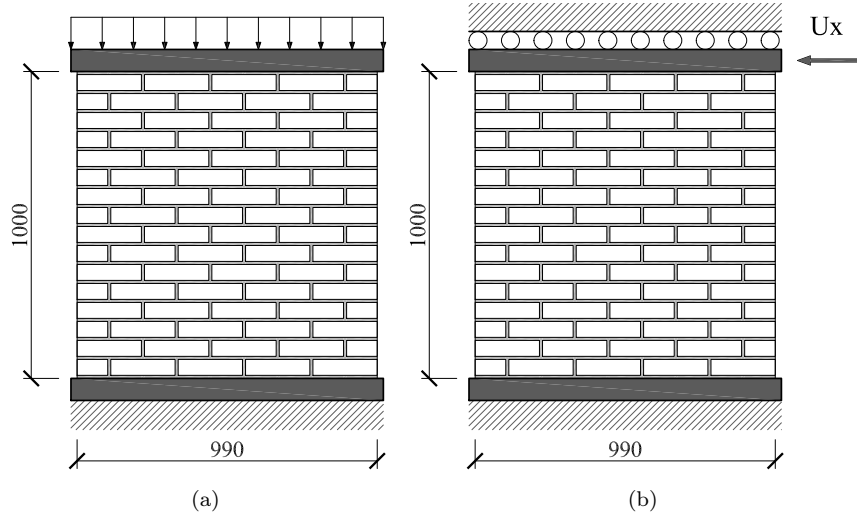


Figure 13: TU Eindhoven shear wall [31]. Geometry and loading conditions: (a) first stage: uniform vertical compression $p = 0.3, 1.21, 2.12\text{ N/mm}^2$; (b) second stage: horizontal displacement.

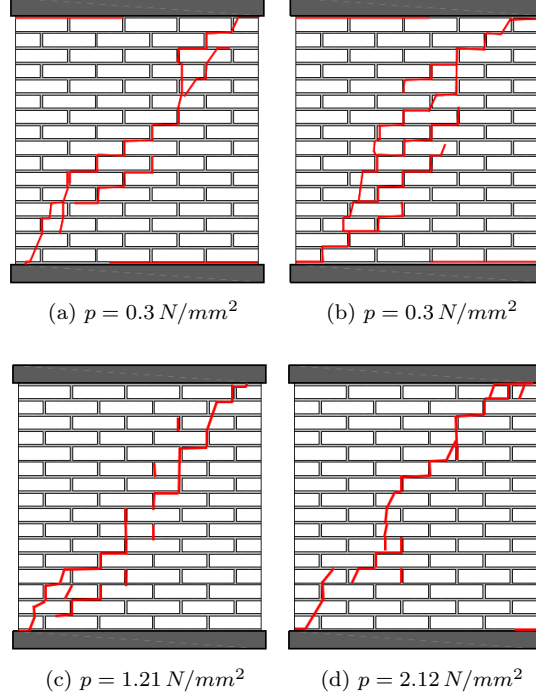


Figure 14: Experimental failure patterns, adapted from [6].

For each one of the three modeling strategies, three analyses have been carried out, one for each level of vertical compression, for a total of nine analyses.

Each nonlinear static analysis is carried out in two stages. During the 1st stage, the top of the wall is subjected to a uniform vertical compression of respectively 0.3 N/mm^2 , 1.21 N/mm^2 and 2.12 N/mm^2 , under load control. During the 2nd stage, a horizontal concentrated force is applied on the top-right corner, via displacement control. The vertical displacement on top of the wall is fixed at the value achieved at the previous time-step.

The pseudo-time is adaptively incremented from $t = 0 \text{ s}$ to $t = 1 \text{ s}$, with an initial time step of $1.0 \times 10^{-2} \text{ s}$, and a minimum time step of $1.0 \times 10^{-9} \text{ s}$. The duration of the two stages are respectively 0.02 s and 0.98 s . In each time step the equilibrium is achieved with a full Newton-Raphson iteration process. Convergence is accepted with a relative tolerance of the residual norm of 1.0×10^{-5} . For all three models, the adopted FEM discretization size is $h = 10.0 \text{ mm}$ (i.e. the thickness of the mortar layer). 4-node displacement-based quadrilateral elements with full 2x2 gauss integration are used for bricks. For the 2D-C and 2D-CD micro-models, the characteristic length used to regularize the softening behavior of the damage model, is equal to the discretization size ($l_{ch} = h = 10.0 \text{ mm}$). In all three models, both the bottom and the top steel beams were modeled, with their corresponding loads and boundary conditions.

6.2. 2D Continuous micro-model (2D-C)

This section reports the results obtained using the 2D-C model. Table 3 shows the material parameters for the damage constitutive model used for both bricks and mortar joints, adapted from the values reported in [6]. Figure 15 shows the obtained force-displacement curves for the three levels of vertical pre-compression. A good agreement with experimental results are obtained, with a slight underestimation of the wall capacity for the highest level of pre-compression. This is probably due to the plane-stress assumption made for both bricks and mortar joints, that becomes hardly applicable to describe the complex interaction between bricks and mortar joints under high levels of compression. A detailed comparison with a full 3D model will be given in Section 6.7. Table 4 shows the obtained results in terms of maximum principal strain, minimum principal stress, tensile and compressive damage.

E	ν	σ_t	G_t	σ_0	σ_p	σ_r	G_c	ε_p	k_b	k_1
850.0	0.15	0.2	0.016	3.0	10.0	2.0	80.0	0.04	1.2	0.16
$\frac{N}{mm^2}$	-	$\frac{N}{mm^2}$	$\frac{N}{mm}$	$\frac{N}{mm^2}$	$\frac{N}{mm^2}$	$\frac{N}{mm^2}$	$\frac{N}{mm}$	-	-	-

(a)

E	ν	σ_t	G_t	σ_0	σ_p	σ_r	G_c	ε_p	k_b	k_1
16700.0	0.15	2.0	0.08	8.0	12.0	1.0	6.0	0.004	1.2	0.0
$\frac{N}{mm^2}$	-	$\frac{N}{mm^2}$	$\frac{N}{mm}$	$\frac{N}{mm^2}$	$\frac{N}{mm^2}$	$\frac{N}{mm^2}$	$\frac{N}{mm}$	-	-	-

(b)

Table 3: Model 2D-C. (a) Material properties for mortar joints (damage model); (b) Material properties for bricks (damage model)

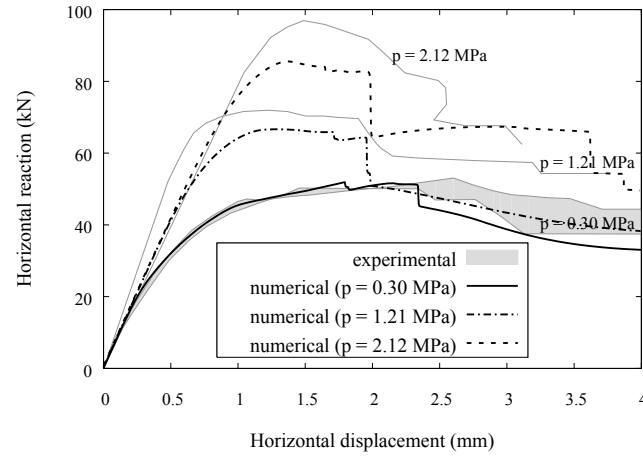


Figure 15: Model 2D-C. load-displacement curves for different values of pre-compression

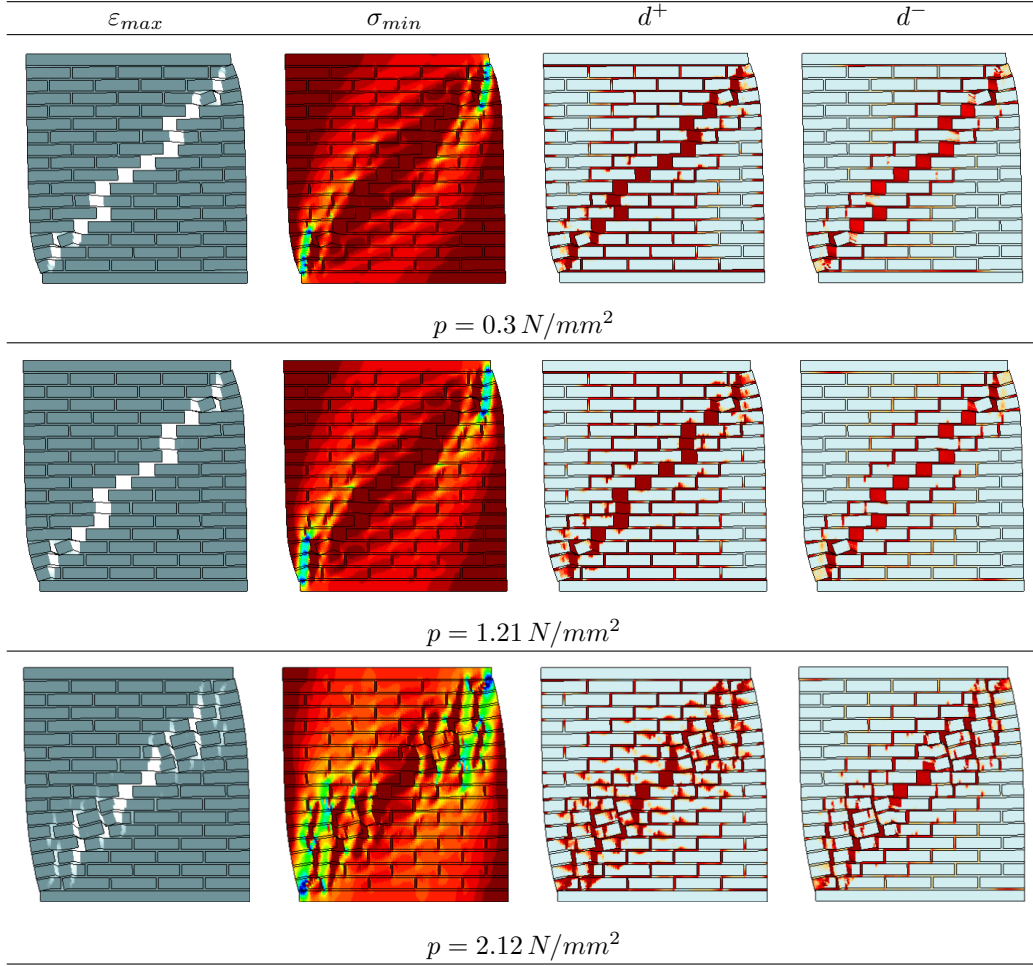


Table 4: Model 2D-C. Results in terms of maximum principal strains, minimum principal stresses, tensile damage and compressive damage, at the ultimate displacement $U_x = 4.0 \text{ mm}$

The results of the model 2D-C for a vertical compression of 0.3 N/mm^2 are carefully commented to explain the behavior of the shear walls and to better understand the evolution of the micro-structure up to the complete failure of the wall. For this reason, five meaningful points of the analysis are considered, identified by instants $t = [0.14, 0.30, 0.47, 0.64, 1.0] \text{ s}$, and by horizontal top-displacements $U_x = [0.5, 1.1, 1.8, 2.5, 4.0] \text{ mm}$. The obtained results are shown in Figure 16, in terms of maximum principal strains. The very first non-linear behavior takes place at a horizontal top-displacement $U_x = 0.5 \text{ mm}$, when horizontal cracks appears at the bottom-right and top-left corners of the wall. At a horizontal top-displacement $U_x = 1.1 \text{ mm}$, staircase cracks emerge from the central part, advancing towards the corners and passing through mortar joints. At this stage, several cracks are visible, but not yet a completely open unique crack. This is

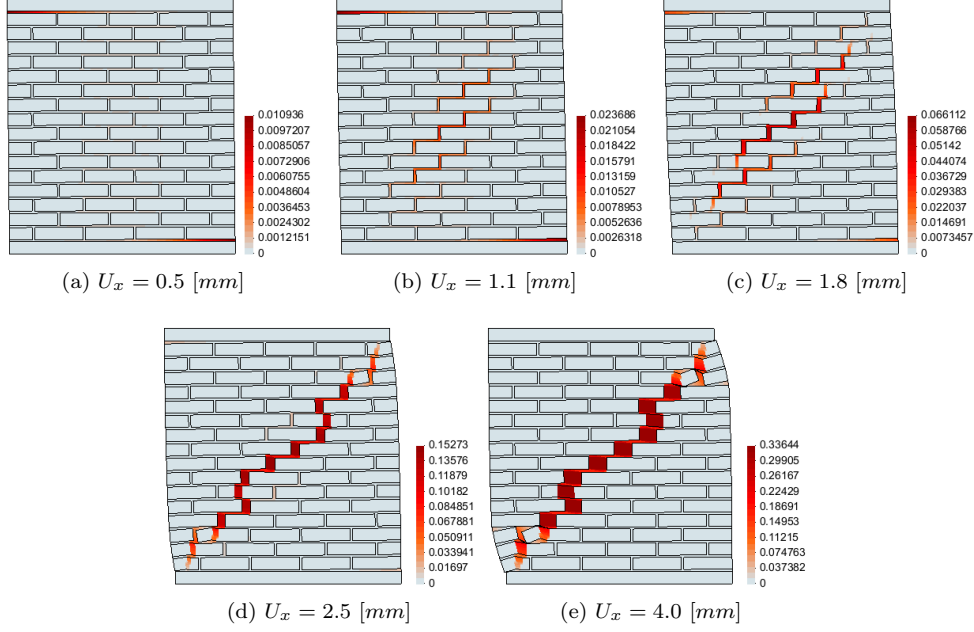


Figure 16: Model 2D-C, $P = 0.3 \text{ N/mm}^2$. Incremental contour plots of maximum principal strain ε_{max}

mainly related to the presence of bricks, whose stress state is still far from their tensile strength. The appearance of these diagonal cracks produces the first significant change in the slope of the global load-displacement curve. At a later stage of the analysis, approximately between top-displacements $U_x = 1.8 \text{ mm}$ and $U_x = 2.5 \text{ mm}$, the tensile strength in some bricks is exceeded, leading to their splitting. As a consequence, the previously mentioned staircase cracks coalesce into a single well defined diagonal cracks. The further opening of this diagonal crack finally leads to the complete development of the shear/crushing mechanism determining the collapse of the wall.

6.3. 2D Discrete micro-model (2D-D)

This section reports the results obtained using the 2D-D model. Table 5 shows the material parameters for the interface constitutive model used for mortar joints, and the elastic properties for the bricks. The potential crack in the bricks have been simulated using a simple damage interface model with a tensile strength $\sigma_t = 2.0 \text{ N/mm}^2$. Figure 17 shows the obtained force-displacement curves for the three levels of vertical pre-compression. Also in this case, a good agreement with experimental results have been reached. As opposed to the 2D-C model, the 2D-D model shows an overestimation of the wall capacity for higher level of pre-compression. This is probably due to assuming only a vertical potential crack in the bricks. This assumption is more appropriate for low values of vertical pre-compression. For higher values of pre-compression, diagonal cracks in the bricks cannot appear, and the main diagonal “crack” has to find its path through the pre-defined

interfaces. Table 6 shows the obtained results in terms of deformed shape, minimum principal stress, tensile/shear and compressive equivalent plastic displacements.

E	ν	k_n	k_s	ν
16700.0	0.15	82.0	36.0	0.15
$\frac{N}{mm^2}$	-	$\frac{N}{mm^3}$	$\frac{N}{mm^3}$	-

(a) (b)

f_t	G_I	c	G_{II}	$\tan\phi$	$\tan\psi$	σ_0	σ_p	σ_r	G_{III}	C_{ss}
0.2	0.016	0.35	0.125	0.75	0	6.0	11.0	2.0	6.0	9.0
$\frac{N}{mm^2}$	$\frac{N}{mm}$	$\frac{N}{mm^2}$	$\frac{N}{mm}$	-	-	$\frac{N}{mm^2}$	$\frac{N}{mm^2}$	$\frac{N}{mm^2}$	$\frac{N}{mm}$	-

(c)

Table 5: Model 2D-D. (a) Material properties for elastic bricks; (b)(c) Material properties for mortar joints (interface model)

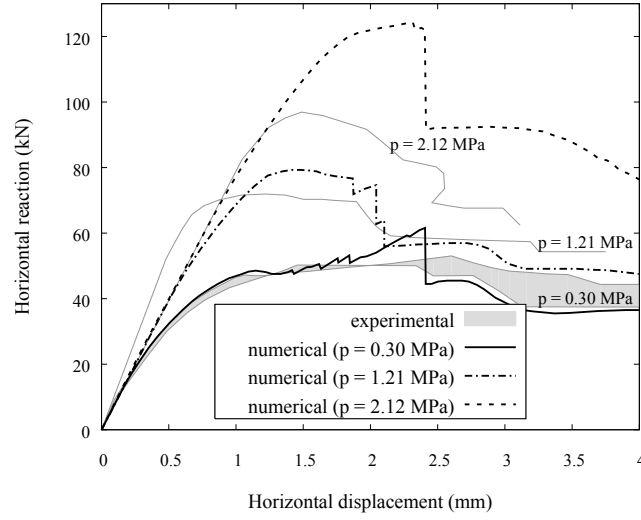


Figure 17: Model 2D-D. load-displacement curves for different values of pre-compression

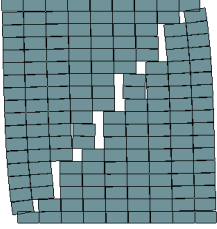
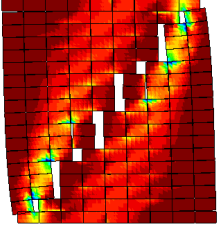
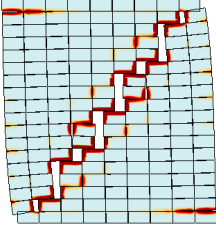
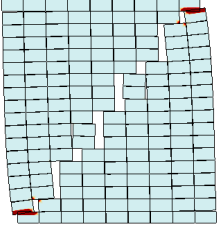
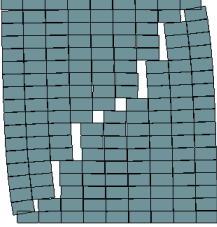
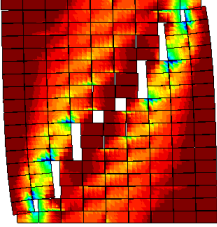
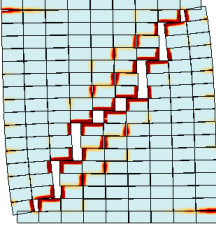
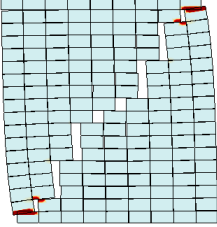
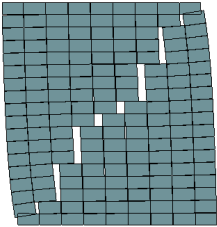
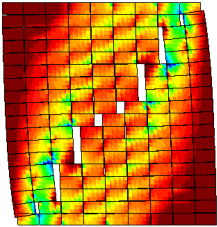
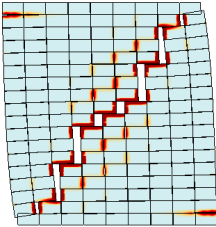
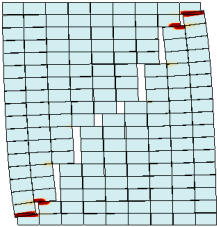
deformed shape	σ_{min}	tensile/shear $u_{p,eq}$	compressive $u_{p,eq}$
			
$p = 0.3 \text{ N/mm}^2$			
			
$p = 1.21 \text{ N/mm}^2$			
			
$p = 2.12 \text{ N/mm}^2$			

Table 6: Model 2D-D. Results in terms of deformed shape, minimum principal stresses, tensile/shear and compressive equivalent plastic displacement, at the ultimate displacement $U_x = 4.0 \text{ mm}$

6.4. 2D Mixed Continuous/Discrete micro-model (2D-CD)

This section reports the results obtained using the 2D-CD model. Table 7 shows the material parameters for the interface constitutive model used for mortar joints, and for the damage model used for the bricks. Figure 18 shows the obtained force-displacement curves for the three levels of vertical pre-compression. A good agreement with experimental results have been obtained also in this case. As expected, this model shows a response which is in-between the 2D-C and the 2D-D models. The overestimation for higher levels of vertical pre-compression is reduced compared to the 2D-D model, by allowing any possible damage pattern in the bricks. Table 8 shows the obtained results

in terms of deformed shape, minimum principal stress, tensile/shear and compressive equivalent plastic displacements.

k_n	k_s	ν
82.0	36.0	0.15
$\frac{N}{mm^3}$	$\frac{N}{mm^3}$	-

f_t	G_I	c	G_{II}	$\tan\phi$	$\tan\psi$	σ_0	σ_p	σ_r	G_{III}	C_{ss}
0.2	0.016	0.35	0.125	0.75	0	6.0	11.0	2.0	6.0	9.0
$\frac{N}{mm^2}$	$\frac{N}{mm}$	$\frac{N}{mm^2}$	$\frac{N}{mm}$	-	-	$\frac{N}{mm^2}$	$\frac{N}{mm^2}$	$\frac{N}{mm^2}$	$\frac{N}{mm}$	-

(a)

E	ν	σ_t	G_t	σ_0	σ_p	σ_r	G_c	ε_p	k_b	k_1
16700.0	0.15	2.0	0.08	8.0	12.0	1.0	6.0	0.004	1.2	0.0
$\frac{N}{mm^2}$	-	$\frac{N}{mm^2}$	$\frac{N}{mm}$	$\frac{N}{mm^2}$	$\frac{N}{mm^2}$	$\frac{N}{mm^2}$	$\frac{N}{mm}$	-	-	-

(b)

Table 7: Model 2D-CD. (a) Material properties for mortar joints (interface model); (b) Material properties for bricks (damage model)

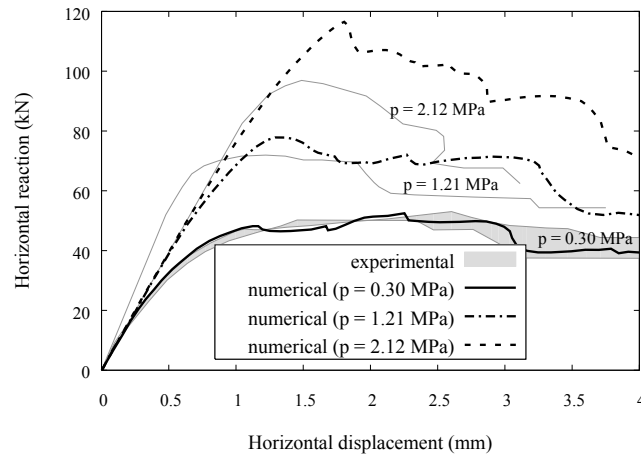


Figure 18: Model 2D-CD. load-displacement curves for different values of pre-compression

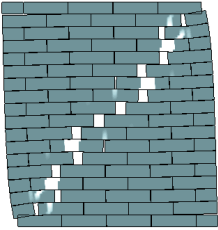
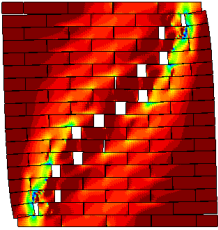
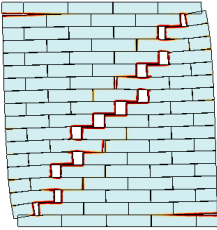
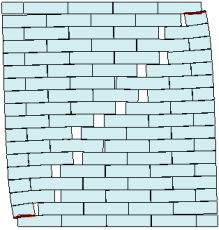
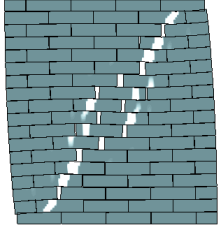
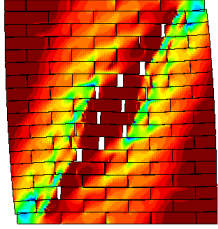
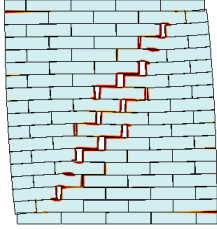
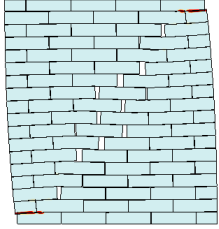
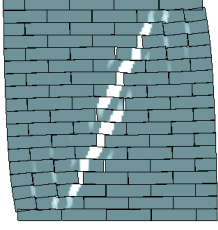
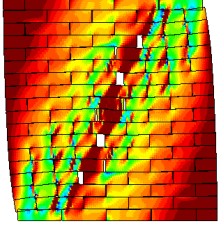
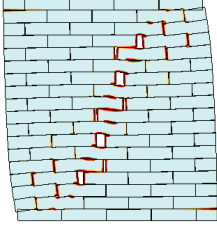
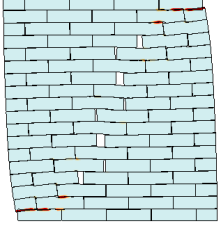
deformed shape	σ_{min}	tensile/shear $u_{p,eq}$	compressive $u_{p,eq}$
			
$p = 0.3 \text{ N/mm}^2$			
			
$p = 1.21 \text{ N/mm}^2$			
			
$p = 2.12 \text{ N/mm}^2$			

Table 8: Model 2D-CD. Results in terms of deformed shape, minimum principal stresses, tensile/shear and compressive equivalent plastic displacement, at the ultimate displacement $U_x = 4.0 \text{ mm}$

6.5. Comparison and discussion of numerical results

The presented results demonstrate that all the three selected models perform relatively well and give similar results, all in good agreement with the experimental tests. Each modeling strategy introduces simplifications with respect to a more general 3D detailed micro-modeling, thus giving slightly different results.

The model 2D-C uses a tension/compression continuum damage model for both bricks and mortar joints. This leads to a very efficient and robust analysis due to the explicit evaluation of the internal variables. The concept of dilatancy (which is of paramount importance for the simulation of shear walls) cannot be easily defined in the context of

damage models, differently from the case of plasticity. Nevertheless, both failure surfaces are active in a tension/compression damage model when the two principal stresses have different sign. In this case, the Cauchy stress is not an isotropic scaling of the effective (elastic) stress. Taking advantage of this feature, a novel compressive model has been formulated to provide a satisfactory shear behavior, in terms of dilatancy and shear strength, as described in Section 4. The proposed model requires a careful definition of the parameter k_1 that sets the shape of the compressive failure surface in the tension/compression quadrants of the principal stresses plane. A value of 0.16 has shown to be adequate for the investigated case studies, see Section 6.6. Also the novel evolution law for the compressive damage variable, based on quadratic Bézier curves, has shown to be adequate for the description of the shear-compression nonlinear response of masonry. The proposed model is remarkably efficient from the point of view of the computation of the constitutive response.

The model 2D-D lumps all the main non-linearity in mortar joints, modeled as interface elements with a composite yield criterion based on the concept of multisurface plasticity. The dilatancy of mortar joints are easily defined due to the non-associativity of the shear mode. Another advantage is that this model separately defines the shear and compressive failure mechanisms. In this way the compressive cap criterion can be used to properly model the compressive behavior of the wall without affecting the shear behavior of the mortar joints. The choice of allowing only the tensile failure of the brick, through a vertical potential crack in the mid-section, limits the number of DOFs of the model, but at the same time it does not allow a natural failure of the bricks when a diagonal crack is likely to appear, as in cases of shear at high compression. It should be mentioned that this model takes into account the reduction in shear strength for high level of compression through the elliptical cap mode. However, this happens at the interface constitutive level but at the structural level the “crack” is forced to find its path through the predefined interfaces. This is probably the cause of overestimation of the strength of the wall for higher vertical compression levels and sudden drops as the vertical cracks in the bricks open, as can be seen in Figure 17.

Finally the model 2D-CD seems to join the features of both the previous models, at the price of a higher computational cost. In this model the accurate description of the mortar joint behavior is achieved with the composite interface model, while the non-linearity in the bricks is described through the continuum damage model, thus without making any assumption on the direction of the cracks in the bricks. Compared to the 2D-D model, the overestimation of the shear strength of the wall under high vertical compression is alleviated, as can be seen in Figure 18.

Slight differences in the crack patterns can be seen by comparing the obtained results for each model and for each level of vertical compression, as shown in Table 9. Model 2D-CD shows a progressively changing direction in the main diagonal crack, becoming more vertical as the vertical compression increases, due to the propagation of diagonal cracks in the bricks, while the model 2D-D shows almost the same failure pattern for all vertical compression levels. Model 2D-C instead shows an overall diagonal crack running from corner to corner, similar to model 2D-D, but with a more diffuse damage pattern in bricks as the vertical compression increases.

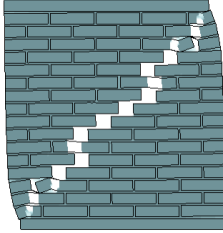
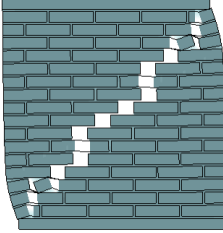
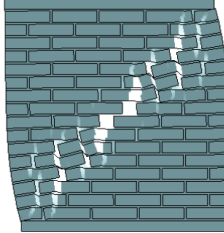
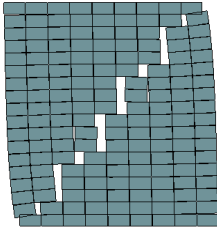
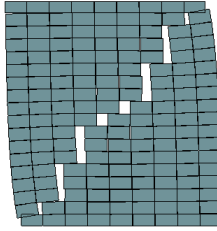
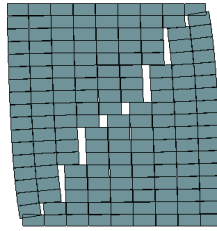
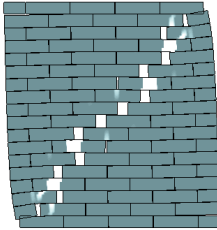
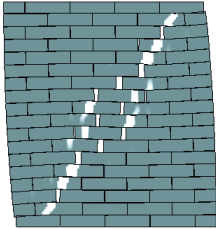
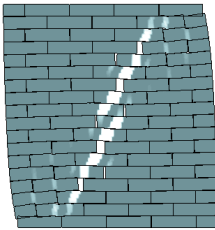
$P = 0.30 \text{ N/mm}^2$	$P = 1.21 \text{ N/mm}^2$	$P = 2.12 \text{ N/mm}^2$
		
2D Continuous micro-model (2D-C)		
		
2D Discrete micro-model (2D-D)		
		
2D Mixed Continuous/Discrete micro-model (2D-CD)		

Table 9: Comparison of failure patterns

Table 10 shows the total simulation time for each one of the analyses with micro-models, carried out with a single standard PC equipped with an Intel Core i7-2670QM CPU and 8 GB RAM. Model 2D-C and model 2D-D are the most efficient ones in terms of computational costs, with model 2D-C giving a slightly better performance. In relative terms, the models 2D-D and 2D-CD provide an increment of the computation time of +23% and + 91% compared with the 2D-C model. The main reason is the efficient formulation typical of damage-models, where the evolution of the internal variables is performed explicitly. On the contrary, the interface model used in model 2D-D is based on multi-surface plasticity (see [6, 5] for further details), where an iterative procedure at the constitutive law level is also necessary in order to integrate the constitutive relation. However, in model 2D-D, this higher cost for the interface constitutive model is amortized by the assumption of an elastic-behavior for bricks. Obviously, model 2D-CD shows the highest computational cost, due to the use of both the interface model for mortar joints,

and the damage model for bricks.

Total simulation time (hh:mm:ss)		
Model 2D-C	Model 2D-D	Model 2D-CD
00 : 09 : 16	00 : 11 : 23	00 : 17 : 41
	+23%	+91%

Table 10: Total simulation time for each one of the three micro-models

6.6. Dilatant behavior in the continuous micro-model 2D-C

This section presents a further assessment of the tension/compression damage model proposed for the 2D-C model. A parametric study is carried out to evaluate the model's capability of handling the dilatant behavior of mortar joints. The effect of the compressive surface on the global response of the wall is evaluated.

For the 2D-C modeling strategy, with the lowest of the three vertical compression levels, 0.3 N/mm^2 , three analyses have been carried out, varying the k_1 parameter in Eq. (5). Three values have been selected: 0.0, 0.16, and 1.0. Recalling that this parameter affects the shape of the compressive surface in tension/compression quadrants, the value of 0.0 leads to a Drucker-Prager criterion, while the value of 1.0 leads to the Lubliner criterion [25]. The intermediate value of 0.16 has been found as optimal for the required dilatancy. The results of the three analyses are shown in Figure 19 in terms of global force-displacement response, and in Figure 20 in terms of maximum principal strains. As expected the Drucker-Prager criterion ($k_1 = 0$) overestimates the dilatancy of the model, and since no vertical displacement is allowed on top of the wall while loaded in shear, this induces an excessive state of compression to the material with a consequent overestimation of the global strength, as well as a more brittle behavior. Furthermore the crack pattern clearly shows how the slip of mortar joints is inhibited, while a unique diagonal crack opens through the bricks. On the contrary, a k_1 value of 1.0 makes the compressive surface very close to the tensile one in the tension/compression quadrants. In this case the dilatancy of mortar joints is not captured at all, and consequently the global shear strength of the model is largely underestimated. The failure in this case is almost only due to slip of mortar joints in the middle of the wall, and only when the crack reaches the boundaries of the wall, it finally propagates vertically through the bricks. On the other hand, the case with $k_1 = 0.16$ provides a more realistic result, by giving a better estimate of the dilatancy of mortar joints.

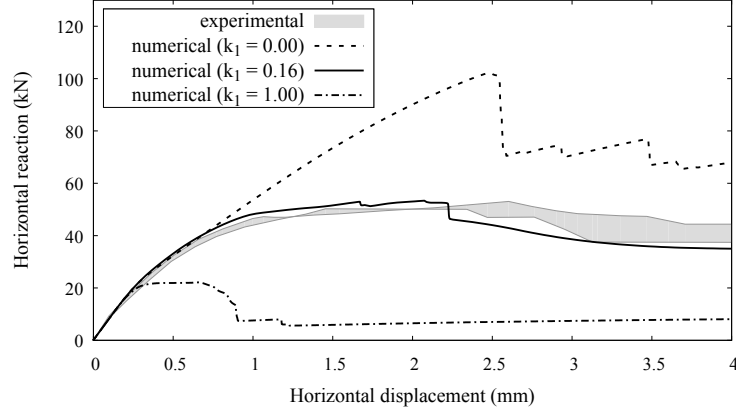


Figure 19: Model 2D-C, $p = 0.3 \text{ N/mm}^2$. Force-displacement curves for three different values of k_1

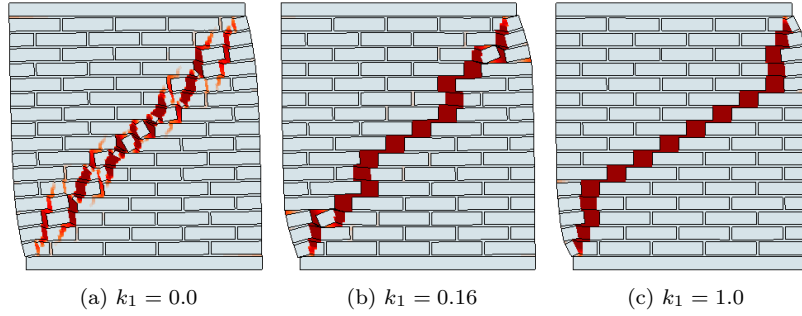


Figure 20: Model 2D-C, $p = 0.3 \text{ N/mm}^2$. Failure patterns for three different values of k_1

6.7. Comparison of 2D-plane stress and full 3D modeling

The adoption of the plane stress hypothesis is widely diffused in the FE analyses of in-plane loaded shear walls [39]. However, as shown in the results presented in Section 6.2, the plane-stress assumption in the model 2D-C, while reducing the computational cost of the simulation, leads to a slight underestimation of the shear strength of walls as the vertical compression level increases. With stiff bricks and soft mortar, high levels of vertical compression induce a state of triaxial compression in mortar joints, thus increasing their strength. This effect is neglected with the plane-stress hypothesis, since the out-of-plane stress is assumed to be zero. This section shows how a full 3D continuous model (3D-C) can provide more accurate results, but at the price of higher computational costs. Another alternative solution that retains the efficiency of 2D modeling is the so called generalized plane state [20, 21].

To account for the increase strength under stress states of triaxial compression, Eq. (9) given for the 2D-plane stress model, should be rewritten for a generic 3D stress state as follows:

$$\tau^- = H(-\bar{\sigma}_{min}) \left[\frac{1}{1-\alpha} \left(\alpha \bar{I}_1 + \sqrt{3} \bar{J}_2 + k_1 \beta \langle \bar{\sigma}_{max} \rangle + \gamma \langle -\bar{\sigma}_{max} \rangle \right) \right] \quad (41)$$

$\gamma \geq 0$ is a material parameter that increases the strength in states of triaxial compression, effectively “enlarging” the damage surface around the hydrostatic axis when all three principal stresses are negative: $\bar{\sigma}_3 \leq \bar{\sigma}_2 \leq \bar{\sigma}_1 = \bar{\sigma}_{max} \leq 0$. In the following simulations this parameter is set equal to 3 (see [25]).

Figure 21 shows, for the case of highest vertical compression level ($p = 2.12 \text{ N/mm}^2$), the load-displacement response of the model 2D-C compared to the respective 3D-C model, while Figure 22 shows the failure pattern obtained from the 3D-C micro-model. As expected, the 3D model shows an improved global response in terms of maximum strength of the wall, while the failure pattern is similar to that obtained from the 2D model.

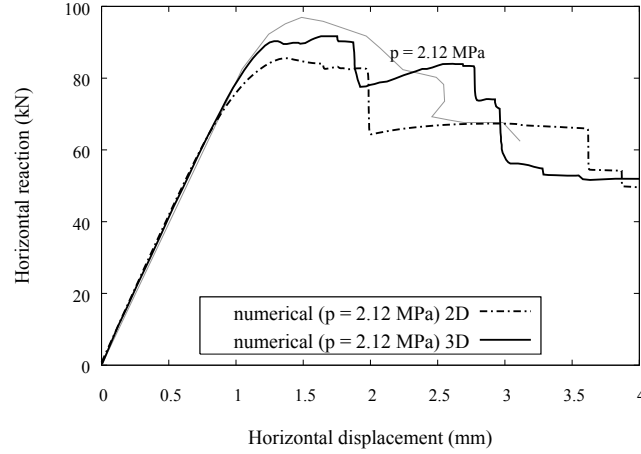


Figure 21: Load-displacement curve of the model 2D-C compared to a full-3D simulation

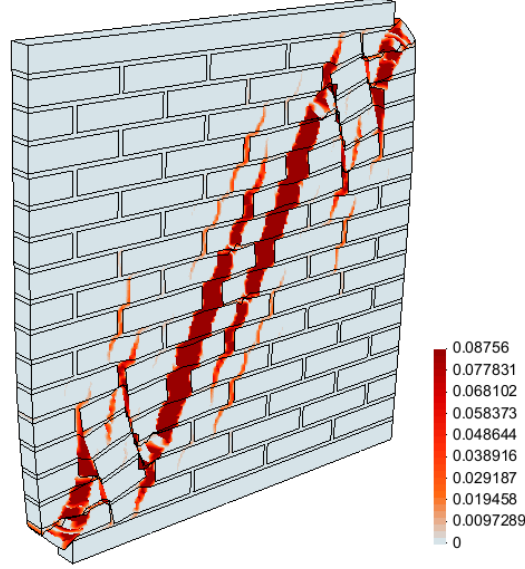


Figure 22: Continuous 3D micro-model (3D-C), maximum principal strain

7. Conclusions

This work has proposed a novel damage-mechanics based micro-model able to represent the nonlinear response of masonry constituents, especially under shear stress states. The presented approach includes the control of the dilatant behavior of the material, even though this aspect is not generally handled by standard continuum damage models. In order to obtain a control on the amount of dilatancy, an existing failure criterion for quasi-brittle materials has been improved under shear conditions and a novel hardening-softening law based on quadratic Bézier curves has been established.

The paper has presented also the critical comparison of the novel continuous micro-modeling technique with well-known discrete micro-modeling strategies for the 2D analysis of in-plane loaded masonry structures. The first numerical strategy, here named 2D Continuous micro-model (2D-C), is based on a classical continuum description of both bricks and mortar joints, both of them treated inelastically using the proposed damage model. The other two strategies, named 2D Discrete micro-model (2D-D) and 2D Mixed Continuous/Discrete micro-model (2D-CD) are already well-known in the literature, and they are based on a discrete description of the micro-structure, modeling bricks with continuum elements and mortar joints with interface elements. Bricks are treated either elastically with potential vertical cracks in the middle vertical section, or inelastically.

The critical analysis of the results has shown how all the investigated strategies are equivalently capable of describing the behavior of shear walls up to their collapse. The main differences have been found with higher compressive levels, where the 2D-D and 2D-CD micro-models overestimate the maximum shear strength of the wall, whereas the 2D-C micro-model slightly underestimates it in a conservative way.

The advantage of the proposed micro-model mainly resides in its simple and efficient format that it inherits from classical damage mechanics models, where the explicit evaluation of the internal variables avoids nested iterative procedures, thus increasing computational performance and robustness. The recurrent disadvantage of standard continuum damage models, i.e. their poor capability of representing the dilatant behavior of mortar joints under shear stress states, has been overcome by the proposed model. Other remarkable advantages offered by the proposed continuous micro-model with a continuum description of both bricks and mortar joints are the simple generation of the finite element model during pre-processing, as well as the straightforward interpretation of the results during post-processing. As regarding the response of the proposed damage model with respect to the dilatant behavior of mortar joints, through the use of the k_1 parameter, future research will be devoted to further assess the reliability of the model on different types of masonry walls.

Acknowledgments

This research has received the financial support from the Graduate School of the University “G. d’Annunzio” of Chieti-Pescara, from the MINECO (Ministerio de Economía y Competitividad of the Spanish Government) through the MULTIMAS project (Multi-scale techniques for the experimental and numerical analysis of the reliability of masonry structures, ref. num. BIA2015-63882-P) and the EACY project (Enhanced accuracy computational and experimental framework for strain localization and failure mechanisms, ref. MAT2013-48624-C2-1-P). Partial financial support by the ReLUIIS (Network of Earthquake Engineering Experimental Laboratories, funded by the Prime Minister Office - Civil Protection Department) project is acknowledged and greatly appreciated. This publication, however, might not necessarily reflect the viewpoint of the Civil Protection Department.

References

- [1] P. Roca, M. Cervera, G. Gariup, L. Pelà, Structural Analysis of Masonry Historical Constructions. Classical and Advanced Approaches, Archives of Computational Methods in Engineering 17 (3) (2010) 299–325, ISSN 1134-3060.
- [2] L. Pelà, M. Cervera, P. Roca, Continuum damage model for orthotropic materials: Application to masonry, Computer Methods in Applied Mechanics and Engineering 200 (9-12) (2011) 917–930, ISSN 0045-7825, URL <http://www.sciencedirect.com/science/article/pii/S0045782510003257>.
- [3] L. Pelà, M. Cervera, P. Roca, An orthotropic damage model for the analysis of masonry structures, Construction and Building Materials 41 (2013) 957–967, ISSN 0950-0618, URL <http://www.sciencedirect.com/science/article/pii/S0950061812004837>.
- [4] L. Pelà, M. Cervera, S. Oller, M. Chiumenti, A localized mapped damage model for orthotropic materials, Engineering Fracture Mechanics 124-125 (2014) 196–216, ISSN 0013-7944, URL <http://www.sciencedirect.com/science/article/pii/S0013794414001386>.
- [5] P. B. Lourenço, J. G. Rots, Multisurface interface model for analysis of masonry structures, Journal of engineering mechanics 123 (7) (1997) 660–668.
- [6] P. B. Lourenço, Computational strategies for masonry structures, Ph.D. thesis, TU Delft, Delft University of Technology, 1996.
- [7] D. V. Oliveira, P. B. Lourenço, Implementation and validation of a constitutive model for the cyclic behaviour of interface elements, Computers & structures 82 (17) (2004) 1451–1461.
- [8] A. Drougkas, L. Pelà, P. Roca, Numerical modelling of masonry shear walls failure mechanisms, in: Proceedings of 9th International Masonry Conference, Guimarães, Portugal, 2014.
- [9] M. Petracca, L. Pelà, R. Rossi, S. Oller, G. Camata, E. Spacone, Regularization of first order computational homogenization for multiscale analysis of masonry structures, Computational Mechanics 57 (2) (2016) 257–276, ISSN 1432-0924, URL <http://dx.doi.org/10.1007/s00466-015-1230-6>.
- [10] M. Petracca, L. Pelà, R. Rossi, S. Oller, G. Camata, E. Spacone, Multiscale computational first order homogenization of thick shells for the analysis of out-of-plane loaded masonry walls, Computer Methods in Applied Mechanics and Engineering 315 (2017) 273–301.
- [11] R. D. Quinteros, S. Oller, L. G. Nallim, Nonlinear homogenization techniques to solve masonry structures problems, Composite Structures 94 (2) (2012) 724–730.
- [12] A. Zucchini, P. Lourenço, A micro-mechanical model for the homogenisation of masonry, International Journal of Solids and Structures 39 (12) (2002) 3233–3255.
- [13] A. Zucchini, P. B. Lourenço, A micro-mechanical homogenisation model for masonry: Application to shear walls, International Journal of Solids and Structures 46 (3) (2009) 871–886.
- [14] M. L. De Bellis, A Cosserat based multi-scale technique for masonry structures, in: PHD Thesis, 2009.
- [15] M. L. De Bellis, D. Addessi, A Cosserat based multi-scale model for masonry structures, International Journal for Multiscale Computational Engineering 9 (5).
- [16] T. J. Massart, Multi-scale modeling of damage in masonry structures, Ph.D. thesis, 2003.
- [17] T. Massart, R. Peerlings, M. Geers, An enhanced multi-scale approach for masonry wall computations with localization of damage, International Journal for Numerical Methods in Engineering 69 (5) (2007) 1022–1059.
- [18] B. Mercatoris, P. Bouillard, T. Massart, Multi-scale detection of failure in planar masonry thin shells using computational homogenisation, Engineering fracture mechanics 76 (4) (2009) 479–499.
- [19] B. Mercatoris, T. Massart, A coupled two-scale computational scheme for the failure of periodic quasi-brittle thin planar shells and its application to masonry, International journal for numerical methods in engineering 85 (9) (2011) 1177–1206.
- [20] D. Addessi, E. Sacco, Nonlinear analysis of masonry panels using a kinematic enriched plane state formulation, International Journal of Solids and Structures 90 (2016) 194–214.
- [21] A. Anthoine, Homogenization of periodic masonry: plane stress, generalized plane strain or 3D modelling?, International Journal for Numerical Methods in Biomedical Engineering 13 (5) (1997) 319–326.
- [22] M. Cervera, J. Oliver, R. Faria, Seismic evaluation of concrete dams via continuum damage models, Earthquake engineering & structural dynamics 24 (9) (1995) 1225–1245.
- [23] R. Faria, J. Oliver, M. Cervera, A strain-based plastic viscous-damage model for massive concrete structures, International Journal of Solids and Structures 35 (14) (1998) 1533–1558.
- [24] J. Y. Wu, J. Li, R. Faria, An energy release rate-based plastic-damage model for concrete, International Journal of Solids and Structures 43 (3) (2006) 583–612.

- [25] J. Lubliner, J. Oliver, S. Oller, E. Oñate, A plastic-damage model for concrete, *International Journal of solids and structures* 25 (3) (1989) 299–326.
- [26] M. L. Raffa, F. Lebon, E. Sacco, H. Welemene, A multi-level interface model for damaged masonry, in: E. B.H.V. Topping, P. Ivanyi (Ed.), "Proceedings of the Fourteenth International Conference on Civil, Structural and Environmental Engineering Computing", Civil-Comp Press, Stirlingshire, UK, 2013.
- [27] E. Sacco, J. Toti, Interface Elements for the Analysis of Masonry Structures, *International Journal for Computational Methods in Engineering Science and Mechanics* 11 (6) (2010) 354–373, URL <http://www.tandfonline.com/doi/abs/10.1080/15502287.2010.516793>.
- [28] C. Citto, Two-dimensional interface model applied to masonry structures, ProQuest, 2008.
- [29] L. Gambarotta, S. Lagomarsino, Damage models for the seismic response of brick masonry shear walls. Part I: The mortar joint model and its applications, *Earthquake Engineering & Structural Dynamics* 26 (4) (1997) 423–439, ISSN 1096-9845.
- [30] H. R. Lotfi, P. B. Shing, Interface model applied to fracture of masonry structures, *Journal of structural engineering* 120 (1) (1994) 63–80.
- [31] T. Raijmakers, A. Vermeltfoort, Deformation controlled tests in masonry shear walls: report B-92-1156, URL <http://books.google.it/books?id=HUmTPgAACAAJ>, 1992.
- [32] Z. Bažant, B. Oh, Crack Band Theory for Fracture of Concrete, BORDAS-DUNOD, URL <http://books.google.it/books?id=x9citwAACAAJ>, 1983.
- [33] J. Oliver, A consistent characteristic length for smeared cracking models, *International Journal for Numerical Methods in Engineering* 28 (2) (1989) 461–474.
- [34] S. Oller, *Fractura Mecánica: Un Enfoque Global*, Ediciones CIMNE y UPC, 2001.
- [35] R. V. D. Pluijm, Shear behavior of bed joints, *Proc. 6 th North American Masonry Conf.* (1993) 125–136.
- [36] P. Dadvand, R. Rossi, E. Oñate, An object-oriented environment for developing finite element codes for multi-disciplinary applications, *Archives of computational methods in engineering* 17 (3) (2010) 253–297.
- [37] P. Dadvand, R. Rossi, M. Gil, X. Martorell, J. Cotella, E. Juanpere, S. R. Idelsohn, E. Oñate, Migration of a generic multi-physics framework to HPC environments, *Computers & Fluids* 80 (2013) 301–309.
- [38] GiD: The personal pre and post preprocessor, 2002.
- [39] S. Saloustros, L. Pelà, M. Cervera, P. Roca, Finite element modelling of internal and multiple localized cracks, *Computational Mechanics* (2016) 1–18.